UC Berkeley
UC Berkeley Previously Published Works

Title
Diffraction imaging of nanocrystalline structures in organic semiconductor molecular thin films

Permalink
https://escholarship.org/uc/item/9750j84r

Journal
Nature Materials, 18(8)

ISSN
1476-1122

Authors
Panova, Ouliana
Ophus, Colin
Takacs, Christopher J
et al.

Publication Date
2019-08-01

DOI
10.1038/s41563-019-0387-3

Peer reviewed

eScholarship.org Powered by the California Digital Library
University of California

Accepted in Nature Materials 4/23/19

Diffraction imaging of nanocrystalline structure in organic semiconductor molecular thin films

Ouliana Panova[1,2,3**], Colin Ophus[3**], Christopher J. Takacs[4], Karen C. Bustillo[3], Luke Ballhorn[5], Alberto Salleo[5], Nitash Balsara[2,6,7], and Andrew M. Minor[1,2,3*]

[1]Department of Materials Science and Engineering, University of California, Berkeley, CA, USA

[2]Materials Science Division, Lawrence Berkeley National Laboratory, Berkeley, CA, USA

[3]National Center for Electron Microscopy, Molecular Foundry, Lawrence Berkeley National Laboratory, Berkeley, CA, USA

[4] SLAC National Accelerator Laboratory, Menlo Park, CA, USA

[5]Department of Materials Science and Engineering, Stanford University. Palo Alto, CA, USA

[6]Department of Chemical and Biomolecular Engineering, University of California, Berkeley, CA, USA

[7]Joint Center for Energy Storage Research, Lawrence Berkeley National Laboratory, Berkeley, CA, USA

[*]Corresponding author: aminor@lbl.gov

[**]These authors contributed equally to this manuscript

Abstract

The properties of organic solids depend on their structure and morphology, yet direct imaging using conventional electron microscopy methods is hampered by the complex internal structure of these materials and their sensitivity to electron beams. Here we managed to observe the nanocrystalline structure of two organic molecular thin film systems using transmission electron microscopy (TEM) by employing a scanning nanodiffraction method that allows for full access to reciprocal space over the size of a spatially localized probe (~2 nm). The morphologies revealed by this technique vary from grains with pronounced segmentation of the structure - characterized by sharp grain boundaries and overlapping domains - to liquid-crystal structures with crystalline orientations varying smoothly over all possible rotations that contain disclinations representing singularities in the director field. The results show how structure-property relationships can be visualized in organic systems using techniques previously only available for hard materials such as metals and ceramics.

Main

The structure and morphology of any functional material can be directly correlated with its properties, including organic solids such as polymers and metal organic frameworks.[1-3] However, direct imaging using conventional electron microscopy methods to study structural ordering at the level of individual defects and nanoscale domains is not routine for organic solids or other soft materials in the same manner as it is for inorganic or hard materials such as metals and ceramics. This difficulty is typically due to the complex (and often hierarchical) internal structure in organic solids and the inherent sensitivity to electron beam induced damage in organic materials. Thus, new and more robust methods for systematically investigating structure are necessary. Towards this end, we demonstrate the 4D-Scanning Transmission Electron Microscopy (4D-STEM) technique[4] for the controlled, systematic, and straight-forward investigation of nano-scale order in hierarchical, organized organic matter systems. As their electronic properties depend highly on their crystallographic geometry, organic semiconductors exemplify the need for improved understanding of the link between structural and functional properties in solid thin-films across a multitude of length-scales ideally suited for study by electron microscopy methods.

The low cost, low density, flexibility, and manufacturability of polymers and organic molecular solids make them attractive materials for applications in photovoltaics[5-7], integrated circuits[8], light-emitting devices[9], bioelectronics, and thermoelectrics, as alternatives to conventional metals and semiconductors. In well-performing organic semiconductors, the molecular structure and processing must both be extensively optimized for a particular application. Intramolecular electronic and excitonic transport is typically directed along the conjugated backbone of a molecular or polymeric system, while intermolecular interactions allow charges and excitons to couple across molecules and travel through larger scales.[10] [11] [12] [13]. It follows that the geometry and configuration of the molecules relative to one another dictate excitation transfer pathways. Understanding how low-dimensional and highly anisotropic semiconductors can form well-connected and robust morphologies remains a great challenge in the manipulation and creation of new topologies for the realization of increasingly efficient charge and energy transport in organic materials.

In this study, we have characterized the nanostructure and defects of two organic semiconductor thin film systems. The first is a small molecule, 7,7'-(4,4 - bis(2 - ethylhexyl) - 4*H* - silolo[3,2-*b*:4, 5-*b*'] dithiophene - 2,6 - diyl) bis(6 – fluoro – 4 - (5'- hexyl[2,2'-bithiophen] - 5 - yl)benzo[*c*][1,2,5] - thiadiazole)[14], classically abbreviated as p-DTS(FBTTh$_2$)$_2$ in the literature, and in this paper denoted as T1, under two different processing conditions using 4D-STEM. The second system is a polymer thin film, Poly[2,5-bis(3-tetradecylthiophen-2-yl)thieno[3,2-b]thiophene] (PBTTT)[15], both in the as-cast and annealed conditions. Our results demonstrate the ability to characterize the structure of organic materials with nanometer resolution using electron microscopy and show how the arrangement of nanoscale domains and their coupling from the nanoscale to mesoscale can be directly visualized for these types of materials systems. This type of information is crucial for building structure-property relationships in this class of materials.

The small molecule under consideration (Fig. 1a) is a well-studied and well-performing electron donor and is responsible for exciton and hole transport when used in conjunction with an acceptor molecule, such as [6,6]-phenyl-C_{70}-butyric acid methyl ester[16] ($PC_{70}BM$) in bulk heterojunction materials with reported efficiencies up to 12% [12,17,18]. The material is known to undergo a lyotropic phase transition during the spin casting process that remains kinetically trapped in the thin film.[19] Polarization-dependent photoconductive AFM was able to map and estimate the local orientational order at a resolution of ~15 nm and complementary dark field TEM experiments confirmed the presence of a liquid crystalline phase at an even coarser resolution.[16] However, due to the intrinsic and practical limitations of both methods, little is known about the structure on the nanometer scale such as the morphology, size, and mutual arrangement of the crystalline domains. When the samples are processed using a small concentration of the co-solvent 1,8-diiodooctane (DIO), the morphology and functional properties are significantly changed. In the poly(3-hexyl-thiophene-2,5-diyl) conducting polymer system it has been observed that the addition of DIO solvent affects a number of morphological and electronic characteristics of the polymer film[20]. Samples treated with certain concentrations of DIO have shown a decreased viscosity and surface roughness under atomic force microscopy[21]. The addition of DIO ultimately appears to contribute to a more compact packing of the donor and acceptor phases and an overall more homogeneous film morphology[22]. When DIO was added to a blend of T1 and $PC_{70}BM$, a maximum photocurrent efficiency (PCE) was found for 0.4% DIO and the addition of $PC_{70}BM$ in large quantities appears to disrupt the crystallinity of T1[23]. Most recently Brown et al. reported that the addition of DIO to a similar donor small molecule converts the normally in-plane direction of the backbone to a 50:50 in-plane:out-of-plane orientation of the backbone[24]. However, the nature and spatial distribution of any morphological changes have yet to be explored at high resolution.

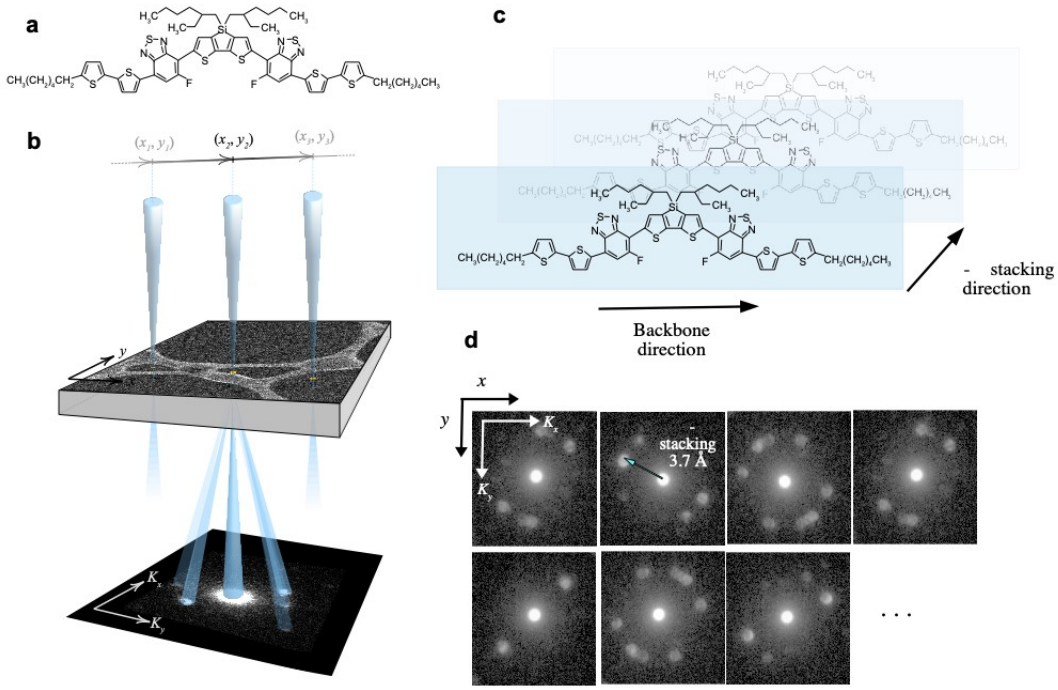

Figure 1. Schematic of the diffraction imaging technique. Molecular structure of the T1 molecule (a) and schematic of the 4D-STEM technique (b). As the convergent beam rasters over the area of interest, a full diffraction pattern is acquired for each real space probe location (*x*, *y*), with a step size large enough to prevent the beam from damaging the yet unsampled neighboring positions. The molecules stack along their π-π bonds as illustrated in (c). The data structure resulting from the technique is shown in (d), with examples of diffraction patterns obtained from T1 + DIO (concentration 0.4%).

Two samples of the T1 molecule, one with DIO treatment (T1+DIO) and one without, were drop-cast and imaged using the 4D-STEM technique, shown schematically in Fig. 1b. The fragile nature of the samples' crystallinity under the electron beam presents a significant challenge, as did the relatively weak diffraction from the ordered domains. In order to reduce beam damage, the samples were cooled with liquid nitrogen and the acquisition parameters were empirically tuned to obtain the best diffraction signal possible; a step size of 10 nm was found to be the limit below which the beam started damaging the crystallinity of sample regions not yet exposed to the electron beam, providing the spatial resolution limit for any image resulting from the data (sample preparation and image acquisition

parameters are detailed in the Methods section). A representative sampling of the diffraction patterns (DPs) obtained are shown in Figure 1d. Most probe locations exhibited at least one diffraction spot pair corresponding to an in-plane ~3.7 Å π-π spacing of the T1 molecule, indicating a textured thin film.

Figure 2 shows how 4D-STEM can extract previously unseen structural information about the small molecule thin film. The traditional high angle annular dark field (HAADF) images acquired during a standard capture (square images in Figures 2a and b) provide effectively no information about the film's structure. Likewise, virtual dark field reconstructions measuring the brightness of an annular ring equivalent to the π-π spacing of the T1 molecule (rectangular images in Figures 2a and b) do not provide any information that can be directly related to the properties of the material. In contrast, the 4D-STEM technique can reveal the underlying structure of the small molecule films by assigning every pixel of a raster scan to a specific in-plane crystal orientation or distribution of crystal orientations[25] (details of the data analysis can be found in the Methods section). Mapping the angle of orientation of the brightest π-π diffraction spot pair for each probe location reveals the impact of DIO on the morphology of the polymer. The sample left to dry without DIO exhibits a structure akin to that of liquid crystals[26], with ordered domains smoothly twisting over the whole 180° range and over length scales ~100 nm (Fig 2c). Of note are the topological defects that can be visualized (indicated by a subset of diffraction patterns in Figure 2g). These singularities represent defect structures called disclinations, which have been extensively modeled[27,28]and previously observed for this system[16]. Figure 2g shows examples of both +1/2 and -1/2 disclinations. Additionally, small overlapping fragments are visible over the entire field of view, with diameters ranging from 10 to 50 nm. The diffraction signal from these grains do not interrupt the larger smoothly twisting grains, indicating that they are located either above or below the primary features.

By contrast, the sample treated with DIO shows a sharply segmented grain structure, with clearly defined grain boundaries and identifiable

domains of closely similar orientations that extend over hundreds of nm, as seen in Figure 2d. While there is still a ~5 -10° internal fluctuation in orientation within the grains due to the flexible nature of the molecule, the crystalline domains are now very clearly defined. Low-angle grain boundaries and small angular fluctuations are known to maintain electronic coupling between neighboring domains better than random orientations[29]. The DPs for this sample also exhibit several distinct lattice reflections at certain probe locations that persist over dozens of real space positions, providing demonstrative evidence that distinct crystalline domains overlap through the film thickness of this sample on the sample size of the probe. While it is not possible to determine the order of the grains along the beam direction (through the thickness of the film), the line plots presented in Figure 2e and f, visualized using flow line methods (often seen in fluid dynamics measurements)[30], allows us to visualize the molecular chains and understand the continuity of the structure, as each lattice reflection found at (x, y) is represented by a line colored and oriented according to its lattice orientation angle θ. The lines in these drawings are oriented perpendicular to their reciprocal space reflections and presumably align with the molecular long axis in real space. While the density of the lines is not indicative of the lattice spacing, their orientation and extent are a direct illustration of the local orientation of the lattice planes, also called the director field[31].

In the T1+DIO sample, many overlapping domains are visible. Most domains tend to be elongated along a direction close to the molecular backbone axis. Most of the larger domains had a longer axial dimension on the order of micrometers, and a shorter axial dimension of 100 – 400 nanometers. Topological singularities were not observed in this sample, but small backbone rotations were observed inside some of the grains (usually <13°). The domains had a slight preferred orientation, but domains stacked along the beam direction did not appear to have any simple crystallographic orientation relationship.

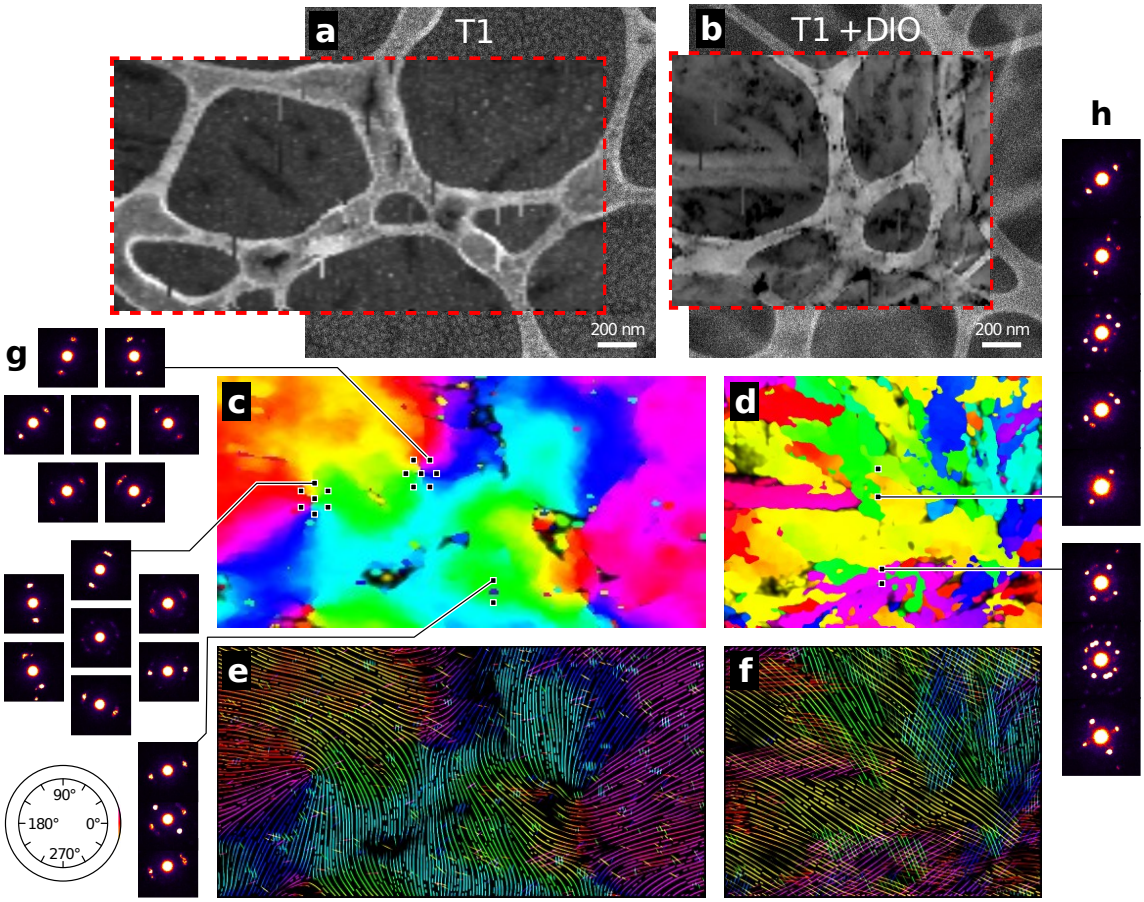

Figure 2. Comparison of grain morphology between DIO samples. The panels on the left (a, c, e, g) are from the sample drop-cast without DIO and the panels on the right (b, d, f, h) are from the sample drop-cast with DIO. (a,b) The background HAADF images show few, if any, of the molecular film details; the web-like features are components of the supporting lacey carbon grid. Dotted lines represent the area over which the 4D-STEM scan was performed. Within the scan areas, a virtual dark field is overlaid onto the HAADF. The orientation maps (c, d) show the direction of the brightest reflection found at that location. Flow line maps (e, f) trace the molecular backbone structure, with the T1 sample demonstrating gradual lattice rotations while the T1+DIO sample shows rigid crystalline domains with significant overlap. (g) Example diffraction patterns from the T1 sample showing disclinations of opposite sign, and an example of a small overlapping fragment. (h) Example diffraction patterns from the T1+DIO showing multiple overlapping grain orientations.

A study of the microstructure of the PBTTT polymer[15] as a function of annealing conditions showcases the potential of the 4D-STEM technique in providing insights in structure-property relationships relevant for organic

field effect transistors. The as-cast carrier mobility of PBTTT in field-effect transistors is on the order of 10^{-2}-0.1 $cm^2/V.s$. PBTTT exhibits a liquid crystalline mesophase in a temperature range determined by the length of its alkyl side-chains. We studied the material having 14 carbon atom long side-chains, which exhibits the mesophase between 140°C and 248°C on heating in the bulk. After annealing the film into the mesophase, the mobility increases up to 1 $cm^2/V.s$ and dramatic microstructural changes are observed by x-ray diffraction and AFM. In particular, annealing leads to an increase in the diffraction signal and the formation of large terraces, indicating an enhancement in order of the material. We fabricated films following the same protocol and thicknesses used to make thin-film transistors and then transferred them to a TEM grid for microstructural characterization. To compare microstructures we studied three conditions: as-cast, annealed in the liquid crystal phase at 160°C, and annealed at 245°C, near the melting point. Long-range shear-induced ordering of the polymer was observed in the melt[32], therefore the latter condition was chosen to determine whether shorter-range order could occur when cooling from the melt in the absence of external shear.

The constructions of flow-line maps as explained earlier reveals dramatic differences in the microstructure at the mesoscale (Figure 3), which are correlated with the charge transport properties of the films. In the as-cast film, no mesoscale order is observed. When annealed in the mesophase, the polymer shows enhanced mesoscale ordering with domains spanning hundreds of nanometers. Interestingly, the regions of order blend smoothly into each other by continuous backbone deformation similar to the T1 sample, clearly seen by comparing Figures 2e and 3f. Orientational correlation is an important functional parameter in PBTTT. Indeed, using polarized soft x-ray scattering, it has been shown that the mobility in PBTTT thin films correlated with backbone orientational correlation[33]. While polarized soft x-rays do not require crystalline material and are a powerful method for investigating orientational order, the dipole nature of the

interaction precludes distinguishing between amorphous material and well-ordered layers overlapping at high angles. In comparison, a 4D-STEM dataset provides additional information on the heterogeneity of the microstructure and can provide a great wealth of quantitative microstructural properties.

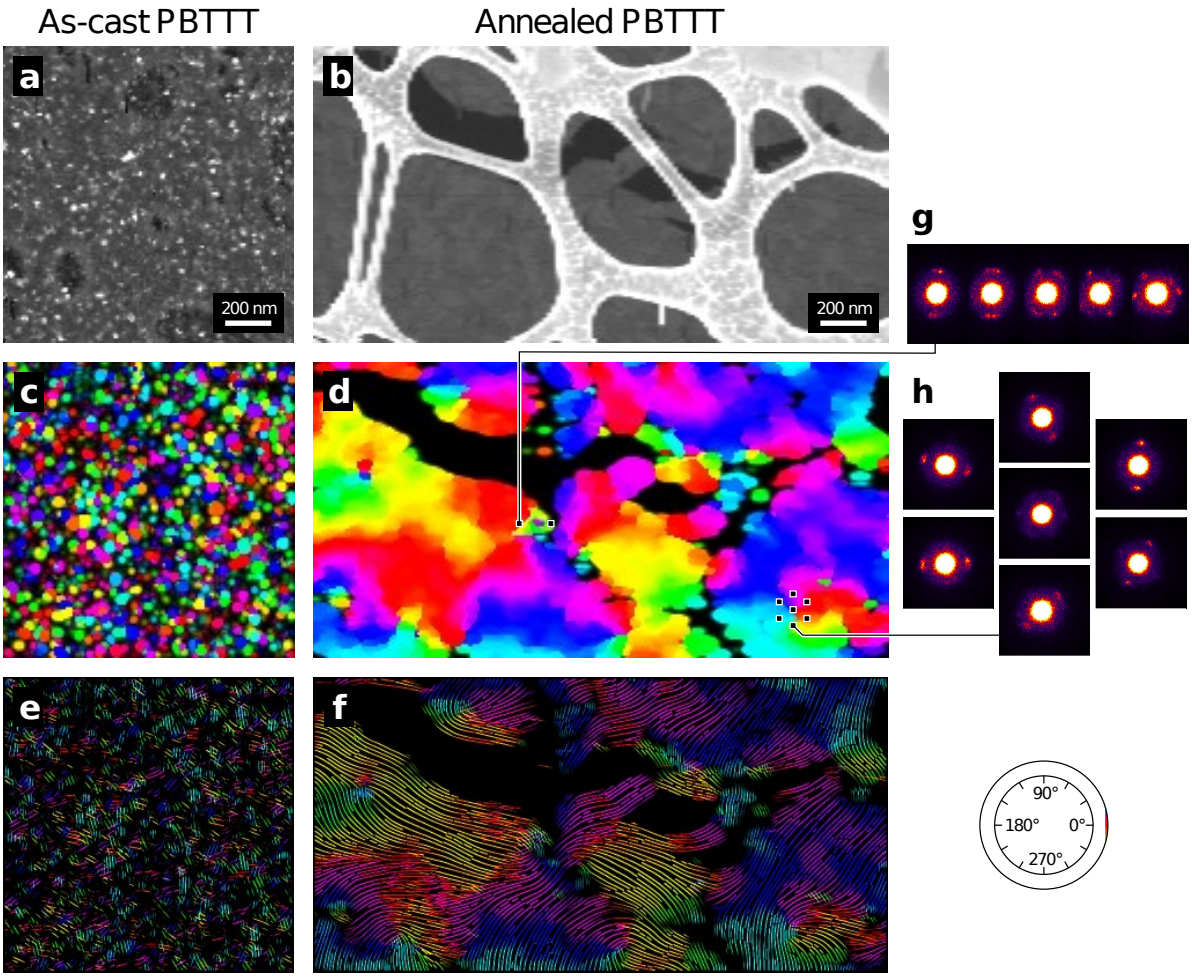

Figure 3: Comparison of grain morphology between PBTTT samples. (a,b) Virtual dark field reconstructions of as-cast and annealed PBTTT thin films, respectively. (c,d) Orientation and (e,f) Flow line maps corresponding to (a,b), respectively. Example diffraction patterns of annealed PBTTT showing (g) overlapping grain orientations and (h) a disclination.

The morphological differences are further emphasized in the autocorrelation study shown in Figure 4. By correlating the lattice orientations at each probe location to those of all other probe locations, a map of the probability of finding the same orientation at a distance Δr and a misorientation $\Delta\theta$ is computed according to the autocorrelation function:

$$C(\Delta r, \Delta\theta) = \frac{\langle I(r,\theta) I(r+\Delta r, \theta+\Delta\theta)\rangle_{r,\theta}}{\langle I(r,\theta)\rangle_{r,\theta}^2}$$

where $I(r,\theta)$ is the measured intensity of the orientation distribution of the lattice vectors, $\langle \ldots \rangle_{r,\theta}$ is an average over all equal radii and orientations, and $\langle I(r,\theta)\rangle_{r,\theta}^2$ represents a normalization factor equivalent to a completely random distribution of lattice orientations in real space. The value of $C(\Delta r, \Delta\theta)$ therefore indicates the correlation between probe locations, with observation probability units relative to a random distribution of orientations. Thus, each vertical slice in Figure 4 represents a histogram of orientation differences at a given separation distance. The red end of the spectrum (C>1) shows orientation differences that are more likely than average to occur. In contrast, the blue end of the spectrum shows angles that are less likely than average to occur – in the small fraction of cases they do occur, it is likely across a grain boundary. Thus, the breakeven point between these two regions, shown as a dashed line in Figure 4, approximates the maximum orientation differences that can be tolerated within a single grain. The slope of this line is then related to the degree of curvature present within grains.

The autocorrelation of the T1 sample in Figure 4a shows a smooth transition in both Δr and $\Delta\theta$, with the spread of $\Delta\theta$ increasing almost linearly with increasing distance Δr. This feature corresponds to the slowly varying orientation of the lattice planes over large distances visible in Figure 2e, and is shown in Figure 4a by a dashed line drawn where the correlation is equal to a random distribution. By contrast, the T1+DIO correlation plotted in Figure 4b shows a sharp drop-off around $\Delta\theta = 15°$, indicating that

misorientations within most grains do not exceed that value. The secondary transition point seen on the T1+DIO map at approximately $\Delta\theta = 30°$ indicates that neighboring and overlapping grains tend to have misorientations below $30° - 40°$ over all distances measured. This can also be seen by the dashed line in Figure 4b, which shows only a small increase with distance indicating that the grains do not contain the varying in-grain orientations measured in Figure 4a. The in-grain lattice plane bending seen in the untreated sample's lattice is the result of a kinetically locked pseudo-phase, and is consistent with the observation that films without DIO dry much faster than ones with DIO[34,35].

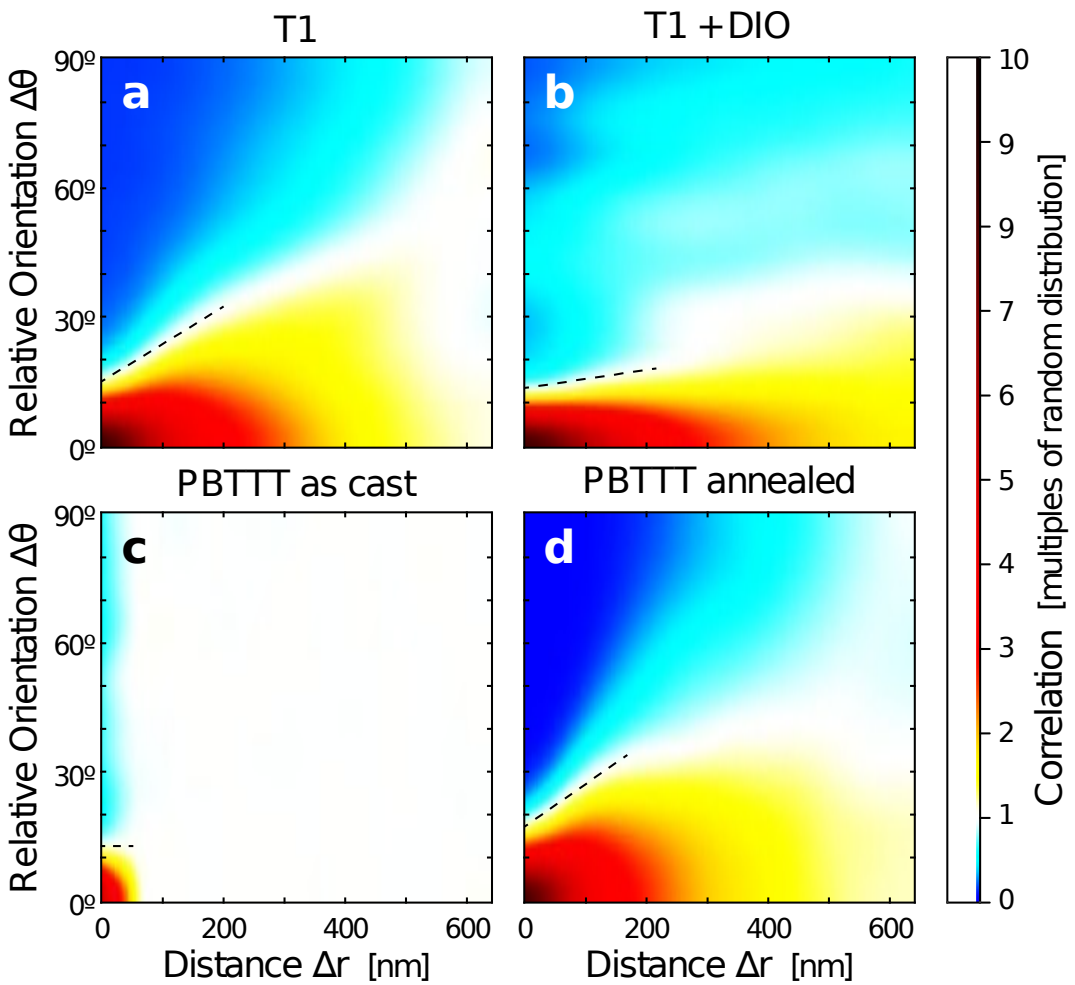

Figure 4. Autocorrelation of the primary lattice vectors over distance Δr and relative orientation $\Delta\theta$, for the films characterized in Figures 2 and 3. Autocorrelation for (a) T1, (b) T1 + DIO, (c) as-cast PBTTT, and (d) annealed PBTTT samples. Correlations are normalized to units of randomly oriented grains, and an overlaid dashed line shows the trend where the measured correlation is equivalent to a random distribution for small distances.

Figure 4c shows the correlation map of the primary lattice for the as-cast PBTTT sample. Beyond distances of Δr = 50 nm, no correlation is visible, which indicates that this sample is composed of small, randomly oriented grains. In comparison, the lattice plane correlation of the annealed PBTTT sample shown in Figure 4d shows very long-range correlations, very similar to those measured for the T1 sample in Figure 4a. This is unsurprising, given the morphological similarities of the structures measured in Figure 2e and 3f. Similarly, the dashed line shown in Figure 4d indicates that the grains have a slowly-varying lattice orientation $\Delta\theta$ which is approximately linear with distance Δr. The correlation measurements in Figure 4 demonstrate that much of a polymer sample's orientation and morphology can be summarized by correlation measurements, which could facilitate their comparison to deposition and growth models.

The ability to simultaneously obtain information at the nm scale and at the mesoscale up to several microns is a very advantageous feature of 4D-STEM over other traditional electron microscopy techniques[36] as charge transport in polymers notoriously depends on processes occurring at many lengthscales[37]. For instance, backbone flow-field maps can be used as the starting point for realistic charge transport simulations, revealing what defects in the films give rise to bottlenecks[38].

We have successfully resolved and mapped the local crystalline nanostructure of two semiconducting small molecule and polymer thin film systems using the 4D-STEM technique. Exposure of the T1 system to DIO

during casting dramatically alters the nanostructure of the resulting material, moving from a smectic liquid crystal-like, continuous, smoothly twisting film to a partially segmented, overlapping discrete grain structure. In the PBTTT system, annealing led to a similar effect. The nanocrystalline morphologies of both systems have been analyzed through automated algorithms in order to gain insight into the differences between the two structures and to relate the structure to the kinetic and energetic pathways of formation. The flexible nature of the 4D-STEM technique, as well as its ability to be applied to any semicrystalline or ordered organic material[39], facilitates measurement and comparison of phase morphology in these organic materials at a spatial resolution not previously possible.

Acknowledgments

Primary funding for the work was provided by the Electron Microscopy of Soft Matter Program from the Office of Science, Office of Basic Energy Sciences, Materials Sciences and Engineering Division of the U.S. Department of Energy under Contract No. DE-AC02-05CH11231. Work at the Molecular Foundry was supported by the Office of Science, Office of Basic Energy Sciences, of the U.S. Department of Energy under Contract No. DE-AC02-05CH11231. LB and AS acknowledge funding from the National Science Foundation DMR Award #1808401. We also thank Dr. Hongping Yan for providing materials and Dr. Mike Toney for useful discussions.

Author Contributions

AM and NB conceived of the project. CT, LB and OP prepared the samples and OP and KB designed the experiment and acquired the data. CO, OP, KB, CT, LB, AS and AM analyzed the data and all authors contributed to the writing of the manuscript.

Competing Financial Interests

The authors declare no competing financial interests.

Data availability

The data that support the findings of this study are available from the corresponding author upon reasonable request.

References

1 Van Krevelen, D. W. & Te Nijenhuis, K. *Properties of polymers: their correlation with chemical structure; their numerical estimation and prediction from additive group contributions*. (Elsevier, 2009).

2 Wilmer, C. E. *et al.* Large-scale screening of hypothetical metal–organic frameworks. *Nature Chemistry* **4**, 83-89 (2012).

3 Fratini, S., Ciuchi, S., Mayou, D., de Laissardière, G. T. & Troisi, A. A map of high-mobility molecular semiconductors. *Nature materials* **16**, 998-1002 (2017).

4 Ophus, C. Four Dimensional Scanning Transmission Electron Microscopy: From Scanning Nanodiffraction to Ptychography and Beyond. *Microscopy and Microanalysis* **in press** (2019).

5 Kim, J. H. *et al.* Optimization and Analysis of Conjugated Polymer Side Chains for High-Performance Organic Photovoltaic Cells. *Advanced Functional Materials* **26**, 1517-1525,(2016).

6 Li, G. *et al.* High-efficiency solution processable polymer photovoltaic cells by self-organization of polymer blends. *Nature Materials* **4**, 864-868, (2005).

7 Zhao, W. *et al.* Fullerene-Free Polymer Solar Cells with over 11% Efficiency and Excellent Thermal Stability. *Advanced Materials* **28**, 4734-4739, (2016).

8 Smits, E. C. P. *et al.* Bottom-up organic integrated circuits. *Nature* **455**, 956-959, (2008).

9 Di, D. *et al.* Efficient Triplet Exciton Fusion in Molecularly Doped Polymer Light-Emitting Diodes. *Advanced Materials* **29**, 1605987, (2017).

10 Salaneck, W. R., Friend, R. H. & Brédas, J. L. Electronic structure of conjugated polymers: consequences of electron–lattice coupling. *Physics Reports* **319**, 231-251, (1999).

11 Collini, E. & Scholes, G. D. Coherent Intrachain Energy Migration in a Conjugated Polymer at Room Temperature. *Science* **323**, 369-373, (2009).

12 Sirringhaus, H. *et al.* Two-dimensional charge transport in self-organized, high-mobility conjugated polymers. *Nature* **401**, 685-688, (1999).

13 Lemaur, V., Steel, M., Beljonne, D., Brédas, J.-L. & Cornil, J. Photoinduced charge generation and recombination dynamics in model donor/acceptor pairs for organic solar cell applications: a full quantum-chemical treatment. *Journal of the American Chemical Society* **127**, 6077-6086 (2005).

14 Zhang, L. *et al.* Poly(3-butylthiophene) Inducing Crystallization of Small Molecule Donor for Enhanced Photovoltaic Performance. *The Journal of Physical Chemistry C* **119**, 23310-23318, (2015).

15 McCulloch, I. *et al.* Liquid-crystalline semiconducting polymers with high charge-carrier mobility. *Nature Materials* **5**, 328, (2006).
16 Takacs, C. J. *et al.* Mapping Orientational Order in a Bulk Heterojunction Solar Cell with Polarization-Dependent Photoconductive Atomic Force Microscopy. *ACS Nano* **8**, 8141-8151, (2014).
17 Dennler, G., Scharber, M. C. & Brabec, C. J. Polymer-fullerene bulk-heterojunction solar cells. *Advanced materials* **21**, 1323-1338 (2009).
18 Zhao, W., Li, S., Zhang, S., Liu, X. & Hou, J. Ternary Polymer Solar Cells based on Two Acceptors and One Donor for Achieving 12.2% Efficiency. *Advanced Materials* **29**, 1604059, (2017).
19 Maged, A. *et al.* Toward Additive-Free Small-Molecule Organic Solar Cells: Roles of the Donor Crystallization Pathway and Dynamics. *Advanced Materials* **27**, 7285-7292,(2015).
20 Arca, F., Loch, M. & Lugli, P. Enhancing Efficiency of Organic Bulkheterojunction Solar Cells by Using 1,8-Diiodooctane as Processing Additive. *IEEE Journal of Photovoltaics* **4**, 1560-1565, (2014).
21 Reichenberger, M. *et al.* Watching Paint Dry: The Impact of Diiodooctane on the Kinetics of Aggregate Formation in Thin Films of Poly(3-hexylthiophene). *Macromolecules* **49**, 6420-6430, (2016).
22 Herath, N. *et al.* Unraveling the Fundamental Mechanisms of Solvent-Additive-Induced Optimization of Power Conversion Efficiencies in Organic Photovoltaic Devices. *ACS applied materials & interfaces* **8**, 20220-20229, (2016).
23 Van Der Poll, T. S., Love, J. A., Nguyen, T. Q. & Bazan, G. C. Non-Basic High-Performance Molecules for Solution-Processed Organic Solar Cells. *Advanced Materials* **24**, 3646-3649 (2012).
24 Brown, S. J. *et al.* Enhancing Organic Semiconductor–Surface Plasmon Polariton Coupling with Molecular Orientation. *Nano letters* **17**, 6151-6156 (2017).
25 Panova, O. *et al.* Orientation mapping of semicrystalline polymers using scanning electron nanobeam diffraction. *Micron* **88**, 30-36, (2016).
26 Frank, F. C. I. Liquid crystals. On the theory of liquid crystals. *Discussions of the Faraday Society* **25**, 19-28 (1958).
27 Meyer, R. B. On the existence of even indexed disclinations in nematic liquid crystals. *Philosophical Magazine* **27**, 405-424, (1973).
28 Saupe, A. Disclinations and Properties of the Directorfield in Nematic and Cholesteric Liquid Crystals. *Molecular Crystals and Liquid Crystals* **21**, 211-238, (2007).
29 Jimison, L. H., Toney, M. F., McCulloch, I., Heeney, M. & Salleo, A. Charge-Transport Anisotropy Due to Grain Boundaries in Directionally Crystallized Thin Films of Regioregular Poly(3-hexylthiophene). *Advanced Materials* **21**, 1568-1572, (2009).
30 Merzkirch, W. *Flow visualization*. (Elsevier, 2012).
31 Wood, B. A. & Thomas, E. L. Are domains in liquid crystalline polymers arrays of disclinations? *Nature* **324**, 655-657, (1986).

32 DeLongchamp, D. M. *et al.* Controlling the Orientation of Terraced Nanoscale “Ribbons” of a Poly(thiophene) Semiconductor. *ACS Nano* **3**, 780-787, (2009).
33 Collins, B. A. *et al.* Polarized X-ray scattering reveals non-crystalline orientational ordering in organic films. *Nature Materials* **11**, 536-543, (2012).
34 Qian, L. *et al.* Effect of Crystallinity of Fullerene Derivatives on Doping Density in the Organic Bulk Heterojunction Layer in Polymer Solar Cells. *Chinese Physics Letters* **32**, 056801 (2015).
35 Yang, X. *et al.* Crystalline Organization of a Methanofullerene as Used for Plastic Solar-Cell Applications. *Advanced Materials* **16**, 802-806 (2004).
36 Takacs, C. J. *et al.* Remarkable Order of a High-Performance Polymer. *Nano Letters* **13**, 2522-2527, (2013).
37 Rivnay, J., Mannsfeld, S. C. B., Miller, C. E., Salleo, A. & Toney, M. F. Quantitative Determination of Organic Semiconductor Microstructure from the Molecular to Device Scale. *Chemical Reviews* **112**, 5488-5519, (2012).
38 Mollinger, S. A., Krajina, B. A., Noriega, R., Salleo, A. & Spakowitz, A. J. Percolation, Tie-Molecules, and the Microstructural Determinants of Charge Transport in Semicrystalline Conjugated Polymers. *ACS Macro Letters* **4**, 708-712, (2015).
39 Mohammadi, E. *et al.* Dynamic-template-directed multiscale assembly for large-area coating of highly-aligned conjugated polymer thin films. *Nature Communications* **8**, 16070, (2017).

Methods

Sample preparation and microscopy

After dissolution of the T1 molecule in chlorobenzene, a 0.4% DIO solution was added to one of the samples before both were drop-cast onto a lacey carbon Cu TEM grid. The PBTTT (Mn = 19 kDa, PDI = 1.3) samples were prepared through spin-casting. Silicon substrates with 200 nm thermal oxide were cleaned by sonicating in acetone, methanol and isopropanol for 15 minutes each. The substrates were then treated with an octyltrichlorosilane self-assembled monolayer after a 20 minute UV-Ozone exposure. Films of PBTTT were spin cast from a 2 mg/mL solution in chlorobenzene. The solution was heated to 80◦C. The films were then spun at 800 rpm for 1 minute. Annealed films were heated for 2 hours at 180◦C, then cooled on a steel heat sink. Spin coating and annealing were performed in a nitrogen glovebox (O2 < 1ppm). Films were transferred onto ultrathin carbon/lacy carbon TEM grids via lift-off in dilute hydrofluoric acid and floating onto an DI water/air interface.

The nanodiffraction datasets were collected using a Gatan Orius CCD on a FEI TitanX microscope at 300 kV operated in STEM mode with a small convergence semi-angle of α=0.48 mrad and a camera length of 380mm. The Gaussian-shaped probe size was measured to be 2.0 nm at full-width half-max. Since the undiffracted central spot was needed for realignment of the diffraction patterns, and to avoid masking any diffraction spots, no beam stop was used. The spots on the diffraction patterns are large in part due to the relatively convergent nature of the beam, and average about 24 pixels in diameter on the detector. Having large but non-overlapping spots on the diffraction pattern presents an advantage when performing template matching, as the locations of the spots can be determined quite robustly.
The samples were cooled with liquid N2 in order to mitigate beam damage to the long-range order during data collection. Because beam exposure of an area destroys its crystallinity, locations for data collection were determined semi-blindly. The sample was surveyed in STEM diffraction mode until a place with strong lattice reflection spots was found, at which point the beam was blanked. The goniometer was then moved by a few microns away from the damaged area, and the 4D-STEM acquisition launched immediately after un-blanking the beam. Diffraction patterns were obtained at an empirically determined minimum step size of 10 nm over an area of 128×128 pixels, with an acquisition time of 33 ms. These parameters were empirically determined to provide the best signal-to-noise ratio on the diffraction patterns. Longer exposure times led to a destruction of sample crystallinity. Shorter step sizes led the beam to prematurely damage areas that had yet to be sampled; even though the probe size at full-width half-max was smaller than the 10 nm step size, the damage incurred by the secondary electrons as they percolate laterally through the sample and cause damage ahead of

the probe put a limit to how close the probe locations could be without seeing the diffraction spots disappear.

The dose or fluence (in e-/A^2) that the sample receives can be estimated using two approaches: (1) Calculate the average dose over the entire scanned area or (2) Calculate the dose as if all the beam current is spread over an area defined by the FWHM of the probe. Using the first method, a beam current of 5 pA with a step size of 10 nm and an exposure of 33 ms translates into an average dose of ~100 e-/A^2 for the nanobeam diffraction experiment in this work. A typical HAADF-STEM image of 50 pA, 12 us dwell time and 2 A pixel size corresponds to a dose of ~1000 e-/A^2. As compared with one STEM image, the nanobeam diffraction exposes the sample to an order of magnitude less dose. Using the second method, a beam current of 5 pA covering the area of a circle of 2 nm (FWHM of probe) with an exposure of 33 ms translates into a dose of ~3E3 e-/A^2 for the nanobeam experiment.

Data analysis

The 4D-STEM data collected was processed in Matlab in order to extract the diffraction spot positions at every pixel. The general peak finding method has been described in a previous publications[25,40]. Because the 4D-STEM experiment covered a relatively large field-of-view, a small linear shift of the diffraction pattern was observed as a function of the probe x and y positions. This shift was measured by fitting the position of the unscattered center disk in all diffraction images, which was set to the origin position $(K_x, K_y)=0$ for each diffraction image. The center disk was averaged (after correcting for origin shifts) and used as a template $I_{ref}(K_x, K_y)$ for hybrid correlation fitting of all scattered and unscattered Bragg disk positions in all images $I(K_x, K_y)$, using the expression

$$P(K_x, K_y)=F^{-1}\left\{\frac{F\left\{I(K_x, K_y)\right\}\circ F\left\{I_{ref}(K_x, K_y)\right\}^{¿}}{\left|F\left\{I(K_x, K_y)\right\}\circ F\left\{I_{ref}(K_x, K_y)\right\}^{¿}\right|^{0.1}}\right\},$$

where local maxima of $P(K_x, K_y)$ represent locations on each diffraction imagewhere the template and the image have a good match. The minimum angular spacing where unique disks with the same diffraction length vector could be identified is approximately 5°. The radial bin width for selecting the d-spacing was +/- 8.5% for the T1 molecule and +/- 10% for the PBTTT.

Trace flow visualizations were made by propagating lines across the field of view. At each real space position r_1 a seed for every found orientation θ_1 is initiated and a line propagated (at a ±90° angle) to its adjoining pixel r_2 , wherein it takes on the orientation θ_2 of the orientation closest to θ_1. The line is stopped if no close orientations are found, or if it overlaps with

previously calculated flow lines (with a relative orientation $\Delta\theta<5°$) within a minimum distance of a few pixels. This procedure generates a field of approximately equally-spaced flowlines, for all orientations detected in each diffraction image. It is also compatible with using multiple Bragg vector spacings, where the flow line spacing can be adjusted to accurately visualize the relative lattice spacings. Note that in the datasets analyzed in this study, the $\pi-\pi$ diffraction spacing was dominant, representing the vast majority of diffracted disk intensity

References for Methods Section:

25 Panova, O. *et al.* Orientation mapping of semicrystalline polymers using scanning electron nanobeam diffraction. *Micron* **88**, 30-36, (2016).

40 Pekin, T. C., Gammer, C., Ciston, J., Minor, A. M. & Ophus, C. Optimizing disk registration algorithms for nanobeam electron diffraction strain mapping. *Ultramicroscopy* **176**, 170-176, (2017).